

See discussions, stats, and author profiles for this publication at: <https://www.researchgate.net/publication/272834006>

Tuning Complex Transition Metal Hydroxide Nanostructures as Active Catalysts for Water Oxidation by a Laser–Chemical Route

ARTICLE *in* NANO LETTERS · FEBRUARY 2015

Impact Factor: 13.59 · DOI: 10.1021/acs.nanolett.5b00026 · Source: PubMed

READS

105

10 AUTHORS, INCLUDING:



Dennis Nordlund

Stanford University

186 PUBLICATIONS 4,605 CITATIONS

[SEE PROFILE](#)



Charles Chauncey Luther Mccrory

California Institute of Technology

17 PUBLICATIONS 634 CITATIONS

[SEE PROFILE](#)



Marca M. Doeff

Lawrence Berkeley National Laboratory

154 PUBLICATIONS 2,969 CITATIONS

[SEE PROFILE](#)



Haimei Zheng

Lawrence Berkeley National Laboratory

59 PUBLICATIONS 2,219 CITATIONS

[SEE PROFILE](#)

Tuning Complex Transition Metal Hydroxide Nanostructures as Active Catalysts for Water Oxidation by a Laser–Chemical Route

Kai-Yang Niu,[†] Feng Lin,[‡] Suho Jung,^{*,⊥} Liang Fang,^{†,¶} Dennis Nordlund,^{||} Charles C. L. McCrory,[⊥] Tsu-Chien Weng,^{||} Peter Ercius,[§] Marca M. Doeff,[†] and Haimei Zheng^{*,†,#}

[†]Materials Sciences Division, [‡]Environmental Energy Technologies Division, and [§]National Center for Electron Microscopy, Lawrence Berkeley National Laboratory, Berkeley, California 94720, United States

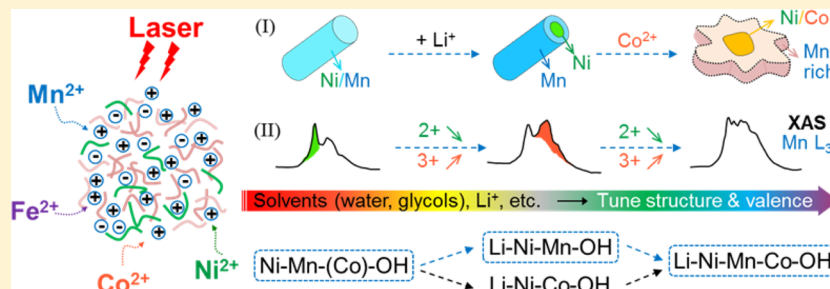
[⊥]Joint Center for Artificial Photosynthesis, California Institute of Technology, Pasadena, California 91125, United States

[¶]State Key Laboratory of Mechanical Transmission, College of Physics, Chongqing University, Chongqing 400044, People's Republic of China

^{||}Stanford Synchrotron Radiation Lightsource, SLAC National Accelerator Laboratory, Menlo Park, California 94025, United States

[#]Department of Materials Science and Engineering, University of California, Berkeley, California 94720, United States

Supporting Information



ABSTRACT: Diverse transition metal hydroxide nanostructures were synthesized by laser-induced hydrolysis in a liquid precursor solution for alkaline oxygen evolution reaction (OER). Several active OER catalysts with fine control of composition, structure, and valence state were obtained including $(\text{Li}_x)[\text{Ni}_{0.66}\text{Mn}_{0.34}(\text{OH})_2](\text{NO}_3)(\text{CO}_3) \cdot \text{mH}_2\text{O}$, $\text{Li}_x[\text{Ni}_{0.67}\text{Co}_{0.33}(\text{OH})_2](\text{NO}_3)_{0.25}(\text{ORO})_{0.35} \cdot \text{mH}_2\text{O}$, etc. An operate overpotential less than 0.34 V at current density of 10 mA cm^{-2} was achieved. Such a controllable laser–chemical route for assessing complex nanostructures in liquids opens many opportunities to design novel functional materials for advanced applications.

KEYWORDS: Transition metal hydroxides, water oxidation, laser chemistry, electrocatalysis, three-dimensional catalyst, volume activity

Water splitting for large-scale production of hydrogen gas is an important strategy for the efficient storage of intermittent renewable energy sources.^{1–3} However, the efficiency of water electrolysis is often constrained by the slow kinetics of one of the half reactions, that is, alkaline oxygen evolution reaction (OER), which requires large overpotentials relative to the hydrogen evolution reaction (HER) to generate appreciable current densities.^{1,2} The search for OER electrocatalysts that operate at high current densities with low overpotentials has resulted in the discovery of numerous transition metal oxides^{2,3} and some transition metal hydr(oxy)-oxides^{4–7} consisting of earth-abundant materials that show decent activities for the OER. The valence states of transition metal ions and the atomic coordination have been considered as important factors for tuning the catalytic activities of these materials.^{8,9} However, it is challenging to control their structures and metal valence states, which makes it difficult to tune the electrocatalytic properties.

To pursue efficient transition metal hydroxide catalysts by design, Markovic et al.⁵ proposed another fundamental

descriptor, that is, $\text{OH}_{\text{ad}}\text{-M}^{2+\delta}$ bond strength, where the overall catalytic activities decline with the increase of $\text{OH}_{\text{ad}}\text{-M}^{2+\delta}$ bond strength (i.e., $\text{OH}-\text{Ni} < \text{OH}-\text{Co} < \text{OH}-\text{Fe} < \text{OH}-\text{Mn}$). Recently, reports suggest that mixed transition metal species with multiple types of catalytic active sites may enhance the overall catalytic properties.^{10,11} And, in general, enhancing the accessibility of reactants to these catalytic active sites could improve the catalytic properties.¹² There is evidence that larger spacing between atomic sites can facilitate the diffusion of H_2O molecules through the material¹³ such as amorphous SiO_2 with silica rings of 6 Å in diameter,¹⁴ graphene layers with 5.5 Å pores,¹⁵ and carbon nanotubes with the inner diameter of 8.14 Å.¹⁶ We propose a three-dimensional catalyst of mixed transition metal ions in which the catalytic sites are distributed throughout the bulk interior during electrocatalysis for OER.

Received: January 4, 2015

Revised: February 11, 2015

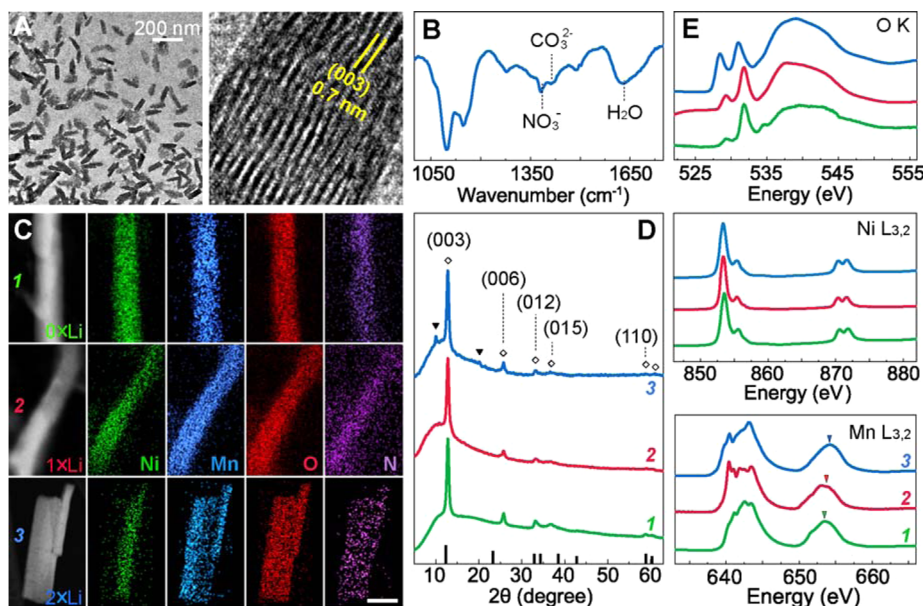


Figure 1. Structure and morphology of (Li)-Ni-Mn-OH nanorods synthesized by laser irradiating aqueous solutions with Li:Ni:Mn ratios of 0:0.5:0.5 (Sample 1), 0.5:0.5:0.5 (Sample 2), and 1.0:0.5:0.5 (Sample 3). (A) Low-magnification and high-resolution TEM images of the nanorods from Sample 2. (B) FT-IR spectrum of the nanorods (Sample 2). (C) STEM images and EDS mapping of the corresponding (Li)-Ni-Mn-OH nanorods of the three samples. The scale bar is 50 nm. (D) XRD patterns of the corresponding (Li)-Ni-Mn-OH nanorods shown in panel C. The reference phase (marked with black lines) is rhombohedral α -nickel hydroxide (JCPDS 380715). The black triangles indicate the Mn-enriched phase in the shell of the Li-Ni-Mn-OH nanorods. (E) Oxygen K-edge, Ni L-edge, and Mn L-edge XAS/TEY spectra of the corresponding (Li)-Ni-Mn-OH nanorods in panel D.

Such three-dimensional catalysts are highly defective hydroxides with distorted layered structure, so the H_2O molecules can either diffuse between the layers or penetrate through the vacancies within the layers for accessing more redox-active metal ion sites in the bulk volume (see the schematic diagram in the Supporting Information, Figure S1).

We use a laser-chemical route with a nanosecond pulsed laser irradiating a precursor solution for accessing those three-dimensional electrocatalysts. Complex metal hydroxide nanostructures with various combinations of transition metal ions (Ni, Co, Fe, Mn, etc.), controlled structures, and tuned metal ion valences were fabricated for efficient alkaline OER. As compared to the conventional coprecipitation approach to fabricate complex hydroxides,¹⁷ where metal ions (M^{d+}) react with hydroxyl ions (OH^-) in an alkaline solution (typically with H_2O_2 as oxidant), which leads to layered double hydroxides formulated as $[M^{z+}]_{1-x}M^{3+}_x(\text{OH})_2]^{d+}(X^{n-})_{q/n} \cdot y\text{H}_2\text{O}$ (in general $Z = 2$, and x is in the range of 0.2–0.33; X stands for the anions located between the metal ion layers), the laser-chemical route has high flexibility in controlling the morphology, structure, composition, and metal valency. This allows us to compare the structure- and valence-state-determined catalytic activities of the complex hydroxides from which optimized complex hydroxide electrocatalysts for the alkaline OER have been achieved.

Herein, we first use different combinations of transition metal ions (Ni, Co, or Mn) to achieve Ni-Mn-OH, Ni-Co-OH, and Ni-Mn-Co-OH compounds. Then, we add the additional Li ions to produce Li-Ni-Mn-OH, Li-Ni-Co-OH and Li-Ni-Mn-Co-OH compounds, inspired by the fact that alkali metal ions (i.e., Li^+) may change the electronic structure and conductivity of electrocatalysts.^{8,11} By changing Li^+ ion concentration in the precursor solutions, we aim to tune the 3D metal valence and thus modify the catalytic activities.

To further manipulate the structure and metal valences of the complex hydroxides, different types of solvents, that is, either water or (tri)ethylene glycol, were used.

By taking (Li)-Ni-Mn-OH as a model system, we first tune the structure of (Li)-Ni-Mn-OH nanostructures by laser irradiating the mixed nitrates aqueous solutions where the Li:Ni:Mn molar ratios of 0:0.5:0.5 (Sample 1), 0.5:0.5:0.5 (Sample 2), or 1.0:0.5:0.5 (Sample 3) were used. Figure 1, panel A shows the typical (Li)-Ni-Mn-OH nanorods synthesized in water (Sample 2). The high-resolution transmission electron microscopy (TEM) image shows that the nanorod has a distorted layer structure with the (003) lattice spacing of ~7 Å. The Fourier transform infrared (FT-IR) spectrum in Figure 1, panel B indicates the existence of nitrate ions (NO_3^-), carbonate ions (CO_3^{2-} , may be generated from the dissolved CO_2 in the solutions), and water molecules in the as-produced compound. The X-ray photoelectron spectroscopy (XPS) spectrum confirms the incorporation of Li ions in the structure (Supporting Information, Figure S2B).

We examined the effect of Li ions on the structural evolutions of the nanorods, shown by the scanning transmission electron microscopy-energy dispersive X-ray spectroscopy (STEM-EDS) mapping in Figure 1, panel C and by X-ray diffraction (XRD) in Figure 1, panel D. The EDS maps display that Ni and Mn ions are distributed uniformly in the nanorods when no Li^+ was added (Sample 1). With the addition of Li^+ in the precursor solution, phase segregation occurs, and core/shell Li-Ni-Mn-OH nanorods with Ni rich in the core and Mn rich in the shell are obtained (Sample 3). An excess of Li^+ ions could generate another Li-enriched shell over the Mn shell (Supporting Information, Figure S3). XRD pattern reveals that the nanorods are isostructural with the rhombohedral α -nickel hydroxide (JCPDS 380715, line markers in Figure 1D), where the d spacing of (003) peak is about 7.0 Å (which is consistent

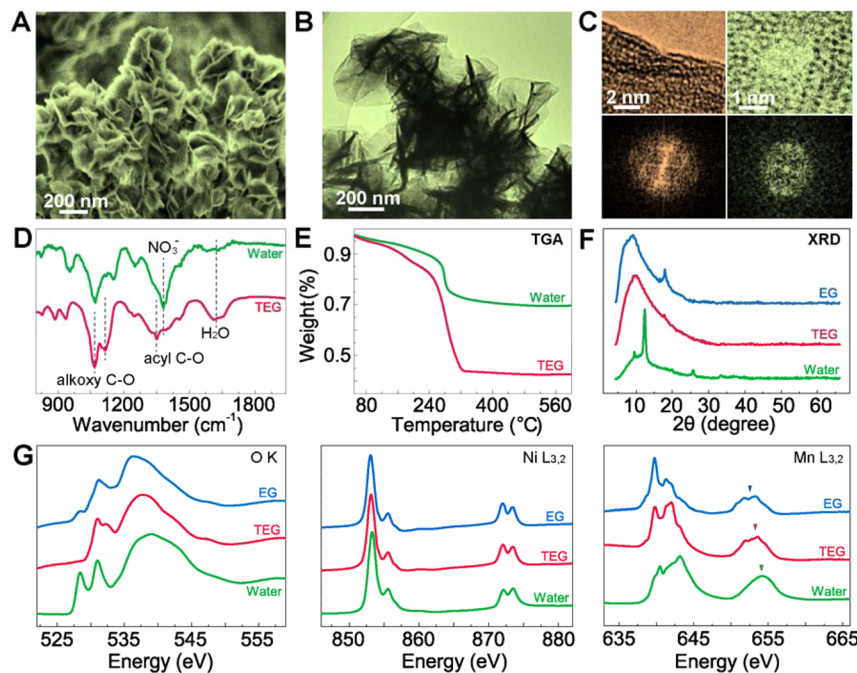


Figure 2. Controllable synthesis of Li–Ni–Mn–OH by laser irradiation of precursor solution in TEG. The precursor solution was prepared by dissolving LiNO_3 , $\text{Ni}(\text{NO}_3)_2$, and $\text{Mn}(\text{NO}_3)_2$ in TEG solutions with the Li:Ni:Mn molar ratio of 1:0.5:0.5. Typically, the production rate in TEG is in the range of 250–350 mg/h. (A) SEM image, (B) low-magnification TEM image, and (C) high-resolution TEM image of the flake-like Li–Ni–Mn–OH, respectively. (D) FT-IR spectra and (E) TGA curves of the as-synthesized Li–Ni–Mn–OH in TEG and water. (F) XRD patterns and (G) O K-edge, Ni L-edge, and Mn L-edge XAS/TEY spectra of the Li–Ni–Mn–OH compounds produced by laser irradiating a precursor solution in TEG, EG, and water. The triangles in panel G show the shifts of the Mn L_2 -edge.

with the structure determined by high-resolution TEM (HRTEM) in Figure 1A). Two additional peaks (d spacing of 0.845 and 0.423 nm; marked as black triangles) are observed in samples with more Li^+ , which indicates a phase mixture. The HRTEM results (Supporting Information, Figure S2C) confirm that, other than the smaller lattice of 7.0 Å, a larger lattice with spacing of 8.4 Å is also identified from the core/shell nanorods in Sample 3, which indicates the lattice expansion of the layered spacing in the Mn-rich shell.

Figure 1, panel E shows the O K-edge, Ni L-edge, and Mn L-edge X-ray absorption spectroscopy total electron yield (XAS/TEY) spectra of the three samples, from which the electronic structures of the metal ions can be identified (see more information in the Supporting Information). From the fine-structure in the L_3 edge, it is clear that the Ni ions are divalent in all three products, but the valence of Mn ions varied significantly.¹⁸ The shift of Mn L_2 edge toward higher energies (marked as triangles in Figure 1E) indicates the increasing of oxidation state of Mn ions. Without lithium (green curve; Sample 1), Mn ions are 3+, similar to what is found in Ni/Mn layered double hydroxides.¹⁷ With the increased Li:(Ni + Mn) molar ratio to 0.5:1.0 (Sample 2), the Mn ions have mixed valences of 2+, 3+, and 4+. When the Li:(Ni + Mn) molar ratio reaches 1.0:1.0, Mn ions are mostly 4+ (Sample 3). Although all oxygen-containing functional groups (e.g., water, nitrate, etc.) within the probing depth will contribute to the O K-edge spectrum, the lowest energy feature (~529 eV) can be uniquely associated with the transition metal derived states in higher valency of Mn.^{19,20} Upon lithiation, we note the distinct increase in this feature and its energetic alignment with MnO_2 .¹⁹ By comparing the pre-edge intensity with the overall O K-edge XAS spectrum, it was seen that Sample 3 shows significantly increased contribution of Mn-hydroxyl at the

surface, which is consistent with the Mn-enriched shell determined by XRD, TEM, and ESD mapping. On the basis of the above analyses, we formulate the series of crystalline complex hydroxide nanorods synthesized in water as $(\text{Li}_x)\text{[Ni}_{0.66}\text{Mn}_{0.34}(\text{OH})_2](\text{NO}_3)(\text{CO}_3) \cdot \text{mH}_2\text{O}$, where the nitrate ions, carbonate ions, and water molecules are likely located between the positively charged metal layers to sustain the stability of the material structure (Supporting Information, Figure S1).

When ethylene glycol (EG) or triethylene glycol (TEG) instead of water is used as solvent, the laser–chemical reactions are drastically different; a polymer-like gel is typically generated after laser irradiation, and an amorphous compound with lower valence states of metal ions is obtained. Figure 2 displays the characteristic features of Li–Ni–Mn–OH compounds synthesized in TEG compared with that synthesized in water and EG. The SEM and TEM images of the powder show nanoflakes with flower-like architecture (Figure 2A,B), where distorted and defective thin layers of the nanoflakes are revealed by the HRTEM image (Figure 2C). In the FT-IR spectra of amorphous Li–Ni–Mn–OH (Figure 2D), besides the nitrate stretching frequency at 1380 cm^{-1} , CO_3^{2-} absorption at 1420 cm^{-1} , and O–H bending of water at 1640 cm^{-1} , the bands at 1091 and 1320 cm^{-1} can be assigned to the C–O stretching of alkoxide ligands and the acyl C–O stretching, respectively. Thermogravimetric analysis (TGA, Figure 2E) shows that the product made in TEG has a much larger weight loss (about 60%) upon heating than that synthesized in water (about 30%). It is likely that extra species, that is, alkoxide ligands, besides water molecules exist in the structure, which results in larger weight loss of the compound synthesized in TEG.

The XRD patterns (Figure 2F) show a broad peak at low angles for the compounds fabricated in glycols, which suggests

the low crystallinity (likely amorphous) of the structure. This is consistent with the structure shown in the HRTEM images (Figure 3C; note that the material produced in EG is composed

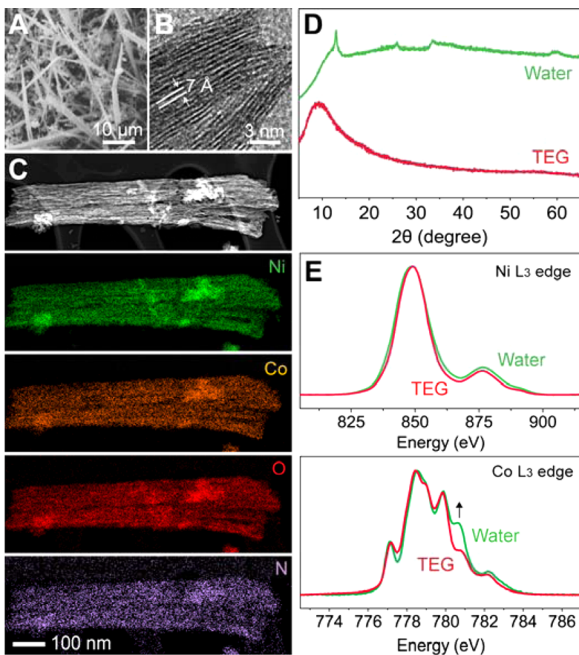


Figure 3. Synthesis of Li–Ni–Co–OH nanocomposites by laser irradiation of precursor solutions with Li:Ni:Co molar ratio of 1.0:0.5:0.5. (A) SEM image and (B) HRTEM image of the as-synthesized Li–Ni–Co–OH nanowires by laser irradiation of the nitrate mixture in water. (C) STEM–EDS profile of the Li–Ni–Co–OH nanowire in panel A. (D) XRD patterns and (E) Ni L₃-edge and Co L₃-edge XAS/TEY spectra of the Li–Ni–Co–OH compounds produced by laser irradiating a precursor solution in water and TEG. The arrow in the Co L₃-edge XAS/TEY spectra indicates the increase of XAS intensity in the Co ions oxidation states at higher energy.

of intertwined thin layers similar to those synthesized in TEG, see Supporting Information, Figure S4). The XAS/TEY spectra (Figure 2G) show that the products obtained from different solutions have distinct valence states. The Ni ions stay as 2+ in all the products, and Mn ions exist mainly as 2+, 3+/2+, and 4+ in EG, TEG, and water, respectively.^{18,21} We note that in the O K-edge XAS spectra of the products made in EG and TEG, no obvious Mn-derived states are present, which indicates the encapsulation of an oxygen-containing species, that is, the alkoxide groups, at the surface. Through the EDS mapping and XAS valency determination, the amorphous hydroxide Li–Ni–Mn–OH synthesized in glycols can be formulated as $\text{Li}_x[\text{Ni}_{0.65}^{2+}\text{Mn}_{0.35-y}^{2+}\text{Mn}_y^{3+}(\text{OH})_2](\text{NO}_3)_{0.19}(\text{ORO})_{0.36} \cdot m\text{H}_2\text{O}$, where the metal ions have disordered coordination and are balanced by hydroxyl (OH^-) and alkoxide ligands ($\text{O}^-\text{R}-\text{O}^-$, $\text{R} = \text{C}_6\text{H}_{12}\text{O}_2$) as well as a small portion of nitrate and carbonate ions.

Furthermore, we replaced the Mn ions with Co ions in the precursor solution to further tune the structure of Li–Ni–Co–OH nanocomposites. Figure 3, panel A shows the SEM image of the as-synthesized Li–Ni–Co–OH nanowires with laser irradiation of an aqueous solution. The HRTEM image (Figure 3B) displays that the nanowire has a layered lattice with *d*-spacing of 0.70 nm. The STEM–EDS analyses (Figure 3C) show that the nanowire is a bundle of nanofibers with Ni, Co, O, and N distributed uniformly in the structure. The XRD

result (Figure 3D) shows that the nanowire has a similar structure to the as-synthesized Li–Ni–Mn–OH nanorods in Figure 1. For comparison, amorphous Li–Ni–Co–OH can also be achieved by laser irradiating the mixed nitrate precursors in TEG (Figure 3D, note that it has a similar flake-like nanostructure with the amorphous Li–Ni–Mn–OH in Figure 2). The XAS spectra (Figure 3E) show that Ni ions stay as 2+ in both the crystalline Li–Ni–Co–OH nanowires and the amorphous Li–Ni–Co–OH nanoflakes, whereas Co ions have distinct oxidation states, which could be assigned to 2+ δ ($0 < \delta < 1$) and 2+ for the crystalline and amorphous Li–Ni–Co–OH nanocomposites, respectively. Accordingly, we could formulate the as-synthesized nanocomposites as $\text{Li}_x[\text{Ni}_{0.80}^{2+}\text{Co}_{0.20}^{2+\delta}(\text{OH})_2](\text{NO}_3)_{0.95} \cdot m\text{H}_2\text{O}$ and $\text{Li}_x[\text{Ni}_{0.67}^{2+}\text{Co}_{0.33}^{3+}(\text{OH})_2](\text{NO}_3)_{0.25}(\text{ORO})_{0.35} \cdot m\text{H}_2\text{O}$ for the crystalline and amorphous Li–Ni–Co–OH, respectively.

By using such a laser–chemical route, we have also achieved many other systems with different combinations of metal ions with high-level control of morphologies, structures, compositions, and valences. By following the same design principles described above, we prepared 12 samples of (Li)–transition metal complex hydroxides with different combinations of transition metal ions, grouped into three categories, that is, (Li)–Ni–Co–OH, (Li)–Ni–Mn–Co–OH, and (Li)–Ni–Mn–OH (Supporting Information, Figures S5 and S6 and Tables S1 and S2). Typically, the products obtained in water are crystalline and those in TEG (or EG) are amorphous (Supporting Information, Figure S5). The metal ions show lower valency in products synthesized in TEG than those in water (Supporting Information, Figure S6). The surface areas for all the catalysts measured from low-temperature Brunauer–Emmett–Teller (BET) surface area testing are in the range of 10–20 m^2/g .

We applied the as-prepared (Li)–transition metal complex hydroxides for electrocatalysis of OER in alkaline solution. As shown in Figure 4, panel A, many of the complex hydroxides show favorable activity and achieve 10 mA cm^{-2} current densities per geometric area at overpotentials of $\eta < 0.4 \text{ V}$. Moreover, most of the materials show good 2-h stability as well; they show relatively little change in operating overpotential at 10 mA cm^{-2} over the course of 2-h constant current polarization (i.e., $\eta_{t=2\text{h}} \leq \eta_{t=0\text{h}}$), as shown in Figure 4, panel B. Some catalysts even show significant enhancements in activity during the 2-h constant polarization. For instance, a steady overpotential of $0.337 \pm 0.007 \text{ V}$ (at 10 mA cm^{-2}) was achieved for the amorphous Ni–Co–OH, which has an initial overpotential of $0.390 \pm 0.008 \text{ V}$ at 10 mA cm^{-2} . Future optimization of the Ni–Co–OH structure may lead to enhanced catalytic performances.

These OER results for the 12 samples with different structures and transition metal valences are summarized in Figure 4, panel C and Supporting Information Tables S1 and S2. Although it is difficult to quantitatively compare the intrinsic activity of these materials with others from the literature due to differences in loading, surface area, conductivity, etc., the activity per geometric area is comparable to several other recently reported catalysts for OER in alkaline solution^{6,11,23,24} (see the comparison with more benchmarking electrocatalysts by the same evaluation methodology in Supporting Information, Figure S7 and Table S3). The results show a trend that the amorphous compounds are generally more active than their crystalline counterparts. This is likely because the amorphous hydroxides are highly defective and

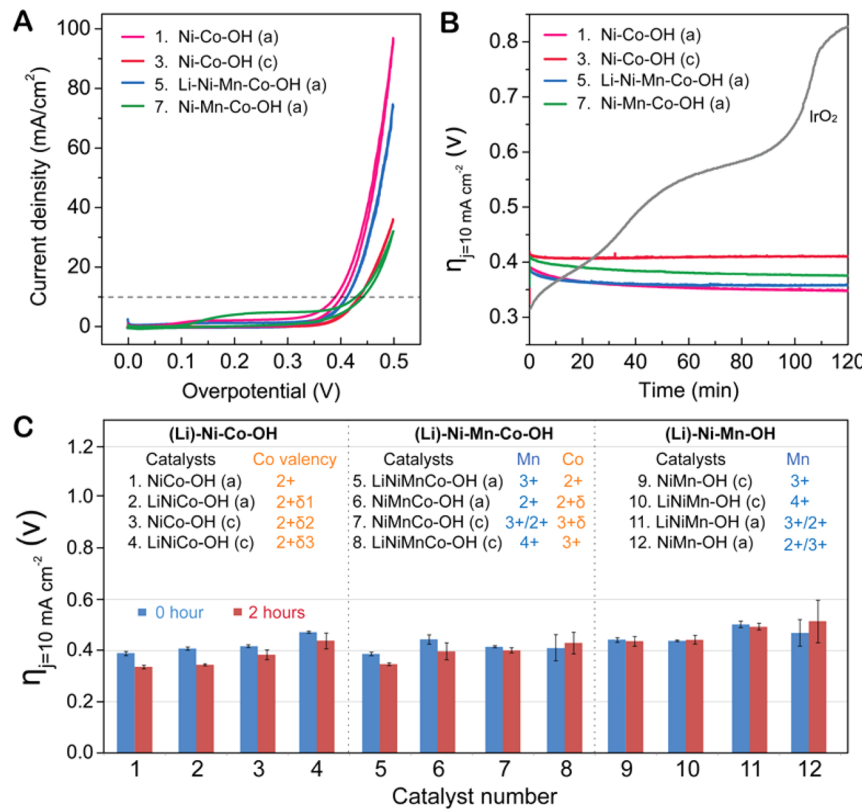


Figure 4. Activity and stability of (Li)-3D metal complex hydroxides for electrocatalysis of alkline OER. (A) Rotating disk voltammograms of electrocatalytic activity for selected four immobilized catalysts. The horizontal dashed line at 10 mA cm^{-2} per geometric area is roughly the current density expected at the anode of a 10% efficient solar water-splitting device operating under 1 sun illumination.^{2,22} The overpotential required to achieve this current density is a convenient figure-of-merit for OER electrocatalysts for possible use in integrated solar water-splitting systems.²³ (B) The 2-h stability plot of the overpotential required to achieve a current density of 10 mA cm^{-2} for four representative catalysts. The 2-h stability of typical IrO₂ catalyst is also plotted here for comparison.²³ (C) Overpotential values required to achieve 10 mA cm^{-2} of 12 catalysts at time = 0 and time = 2 h with standard deviation. The average overpotential required to achieve 10 mA cm^{-2} per geometric area after 2 h of constant electrolysis ($\eta_{t=2h}$) is reported for each catalyst along with standard deviations measured with at least three independently prepared catalytic surfaces. Note: the crystalline catalysts are labeled with "(c)", and the amorphous ones are labeled with "(a)". The variable δ_x ($0 < \delta_x < 1$) is used to describe the valence differences where $\delta_1 < \delta_2 < \delta_3$ is noted.

hydroxyl-deficient, the unsaturated sites and disordered coordination of metal ions are dominant. As a result, the water molecules can either diffuse between the distorted layers or penetrate through vacancies within the layers, which makes a great number of metal ions even in the bulk interior redox-active (see the structure scheme in Supporting Information, Figure S1). The three-dimensional catalyst enhances the overall catalytic activities as a comparison to the conventional surface catalysts.

In view of the metal valency as a catalytic descriptor, our results suggest that Co²⁺ and Mn³⁺ are the active sites in (Li)-Ni-Co-(Mn)-OH nanostructures for the alkaline OER (Figure 4C). This is also consistent with the reports of the active sites in other complex materials, such as Mn³⁺ in delithiated Li_{2-x}MnP₂O₇⁸ and high-spin Co²⁺ in distorted prisms in perovskite oxide,⁹ which act as much active sites for the electrocatalysis of alkaline OER. Incorporation of Li⁺ in the complex hydroxide nanostructures can promote the Mn and Co ions to their higher valence states (Supporting Information, Figure S6) and lead to lower activities of the materials for OER (Figure 4C). This agrees with the previous reports in other Li-containing complex metal oxide OER catalysts where lower activities were obtained in the lithiated materials.^{11,25} The Li ions can be mobile, which may induce structure change of the

catalysts during the OER reaction. The possible structural changes of the hydroxide catalysts need further investigations.

In conclusion, we have demonstrated a laser-chemical protocol for accessing various complex transition metal hydroxides with well-controlled structures and metal valences as electrocatalysts for alkaline OER. Different combinations of transition metal (Ni, Mn, or Co) hydroxide nanostructures with or without alkali metal ions (Li⁺) are achieved from the laser-mediated hydrolysis reactions. The type of solvents, either water or TEG (EG), affects the structure and metal valency of the hydroxides, where the products obtained in aqueous solutions are crystalline, but those in glycols tend to be amorphous. The valence states of the metal ions in the nanocomposites produced in aqueous solutions tend to be higher than that in glycol solutions, for example, the Mn ions stay as 4+ and 3+, and Co ions are 3+ and 2+ in the Li-Ni-Mn-Co-OH compounds synthesized in water and TEG, respectively. In addition, Li⁺ can also tune the structure and metal valency. Compositional segregation of Ni and Mn occurs with the increase of Li⁺ dose in the (Li)-Ni-Mn-OH compound, which results in core-shell nanorods with Ni in the core and Mn in the shell; meanwhile, the Mn ion valence is increased from 3+ to 4+. The as-synthesized complex metal hydroxide nanocomposites have highly defective and distorted layered structures, which form a new class of three-dimensional

electrocatalysts for alkaline OER. This flexible, controllable, and scalable laser–chemical process opens up a new avenue for the design of novel complex materials with advanced functionalities.

■ ASSOCIATED CONTENT

Supporting Information

Experimental details and characterizations of EDS mapping, TEM images, XRD, and XAS of the as-prepared materials. This material is available free of charge via the Internet at <http://pubs.acs.org>.

■ AUTHOR INFORMATION

Corresponding Authors

*suho.jung@caltech.edu.
*hmzheng@lbl.gov.

Author Contributions

The manuscript was written through contributions of all authors. All authors have given approval to the final version of the manuscript. F.L., S.J., and L.F. contributed equally.

Notes

The authors declare no competing financial interest.

■ ACKNOWLEDGMENTS

We thank Prof. Alexis T. Bell and Dr. Mary W. Louie for useful discussions. We performed TEM characterization using Tecnai, TitanX, and TEAM1 microscopes at National Center for Electron Microscopy of the Molecular Foundry at Lawrence Berkeley National Laboratory (LBNL), which is supported by the U.S. Department of Energy (DOE) Office of Basic Energy Sciences under Contract No. DE-AC02-05CH11231. The synchrotron X-ray portions of this research were carried out at the Stanford Synchrotron Radiation Lightsource (Beamlines 10-1 and 8-2), a Directorate of SLAC National Accelerator Laboratory and an Office of Science User Facility operated for the U.S. Department of Energy Office of Science at Stanford University. Electrochemical measurements are based on work performed at the Joint Center for Artificial Photosynthesis, a DOE Innovation Hub, supported through the Office of Science of the U.S. DOE under Award No. DE-SC0004993. K.N. acknowledges Dr. Renjia Zhou for performing the TGA, FT-IR in Molecular Foundry and Dr. Xin Liu at LBNL for measuring the UV-vis absorption spectra. L.F. acknowledges the support of China Scholarship Council (CSC) under No. 2010850533 and the National Basic Research Program of China (2014CB931700). F.L., D.N., and T.-C.W. thank Dr. Jun-Sik Lee and Glen Kerr for the help at SSRL Beamline 8-2. H.Z. acknowledges the SinBeRise program of BEARS at University of California, Berkeley for travel support. She also thanks the support of DOE Office of Science Early Career Research Program.

■ REFERENCES

- (1) Lewis, N. S.; Nocera, D. G. *Proc. Natl. Acad. Sci. U. S. A.* **2006**, *103* (43), 15729–15735.
- (2) Walter, M. G.; Warren, E. L.; McKone, J. R.; Boettcher, S. W.; Mi, Q.; Santori, E. A.; Lewis, N. S. *Chem. Rev.* **2010**, *110* (11), 6446–6473.
- (3) Cook, T. R.; Dogutan, D. K.; Reece, S. Y.; Surendranath, Y.; Teets, T. S.; Nocera, D. G. *Chem. Rev.* **2010**, *110* (11), 6474–6502.
- (4) Gao, M.; Sheng, W.; Zhuang, Z.; Fang, Q.; Gu, S.; Jiang, J.; Yan, Y. *J. Am. Chem. Soc.* **2014**, *136* (19), 7077–7084.
- (5) Subbaraman, R.; Tripkovic, D.; Chang, K.-C.; Strmcnik, D.; Paulikas, A. P.; Hirunsit, P.; Chan, M.; Greeley, J.; Stamenkovic, V.; Markovic, N. M. *Nat. Mater.* **2012**, *11* (6), 550–557.
- (6) Song, F.; Hu, X. *Nat. Commun.* **2014**, *5*, 4477.
- (7) Hunter, B. M.; Blakemore, J. D.; Deimund, M.; Gray, H. B.; Winkler, J. R.; Müller, A. M. *J. Am. Chem. Soc.* **2014**, *136* (38), 13118–13121.
- (8) Park, J.; Kim, H.; Jin, K.; Lee, B. J.; Park, Y.-S.; Kim, H.; Park, I.; Yang, K. D.; Jeong, H.-Y.; Kim, J.; Hong, K. T.; Jang, H. W.; Kang, K.; Nam, K. T. *J. Am. Chem. Soc.* **2014**, *136* (11), 4201–4211.
- (9) Grimaud, A.; Carlton, C. E.; Risch, M.; Hong, W. T.; May, K. J.; Shao-Horn, Y. *J. Phys. Chem. C* **2013**, *117* (49), 25926–25932.
- (10) Smith, R. D.; Prévot, M. S.; Fagan, R. D.; Zhang, Z.; Sedach, P. A.; Siu, M. K. J.; Trudel, S.; Berlinguet, C. P. *Science* **2013**, *340* (6128), 60–63.
- (11) Lu, Z.; Wang, H.; Kong, D.; Yan, K.; Hsu, P.-C.; Zheng, G.; Yao, H.; Liang, Z.; Sun, X.; Cui, Y. *Nat. Commun.* **2014**, *5*, 4345.
- (12) Cocke, D. *J. Met.* **1986**, *38* (2), 70–75.
- (13) Thallapally, P. K.; Lloyd, G. O.; Atwood, J. L.; Barbour, L. J. *Angew. Chem.* **2005**, *117* (25), 3916–3919.
- (14) Kostinski, S.; Pandey, R.; Gowtham, S.; Pernisz, U.; Kostinski, A. *IEEE Electron Device Lett.* **2012**, *33* (6), 863–865.
- (15) Cohen-Tanugi, D.; Grossman, J. C. *Nano Lett.* **2012**, *12* (7), 3602–3608.
- (16) Ye, H.; Zhang, H.; Zheng, Y.; Zhang, Z. *Microfluid. Nanofluid.* **2011**, *10* (6), 1359–1364.
- (17) Zhou, F.; Zhao, X.; van Bommel, A.; Rowe, A. W.; Dahn, J. R. *Chem. Mater.* **2009**, *22* (3), 1015–1021.
- (18) Pecher, K.; McCubbery, D.; Kneedler, E.; Rothe, J.; Bargar, J.; Meigs, G.; Cox, L.; Nealson, K.; Tonner, B. *Geochim. Cosmochim. Acta* **2003**, *67* (6), 1089–1098.
- (19) De Groot, F.; Grioni, M.; Fuggle, J.; Ghijssen, J.; Sawatzky, G.; Petersen, H. *Phys. Rev. B* **1989**, *40* (8), 5715.
- (20) Gilbert, B.; Frazer, B.; Belz, A.; Conrad, P.; Nealson, K.; Haskel, D.; Lang, J.; Srajer, G.; De Stasio, G. *J. Phys. Chem. A* **2003**, *107* (16), 2839–2847.
- (21) Lin, F.; Markus, I. M.; Nordlund, D.; Weng, T.-C.; Asta, M. D.; Xin, H. L.; Doeffer, M. M. *Nat. Commun.* **2014**, *5*, 3529.
- (22) Gorlin, Y.; Jaramillo, T. F. *J. Am. Chem. Soc.* **2010**, *132* (39), 13612–13614.
- (23) McCrory, C. C.; Jung, S.; Peters, J. C.; Jaramillo, T. F. *J. Am. Chem. Soc.* **2013**, *135* (45), 16977–16987.
- (24) Suntivich, J.; May, K. J.; Gasteiger, H. A.; Goodenough, J. B.; Shao-Horn, Y. *Science* **2011**, *334* (6061), 1383–1385.
- (25) Maiyalagan, T.; Jarvis, K. A.; Therese, S.; Ferreira, P. J.; Manthiram, A. *Nat. Commun.* **2014**, *5*.